Measurement Science
and Technology

PAPER

Measurement of dynamic deformation during shock loading using a fiber-optic loop-sensor

To cite this article: Yang Baohui *et al* 2025 *Meas. Sci. Technol.* **36** 015124

IOP Publishing Measurement Science and Technology
Meas. Sci. Technol. **36** (2025) 015124 (9pp) https://doi.org/10.1088/1361-6501/ad8ee6

Measurement of dynamic deformation during shock loading using a fiber-optic loop-sensor

Yang Baohui[1,2], **Dung Dinh Luong**[1,*] **and Nikhil Gupta**[1]

[1] Composite Materials and Mechanics Laboratory, Mechanical and Aerospace Engineering Department, New York University, Tandon School of Engineering, Brooklyn, NY 11201, United States of America
[2] Guangxi University of Science and Technology, 2 Wenchang Road, Chengzhong District, Liuzhou, Guangxi, People's Republic of China

E-mail: dluong@nyu.edu

Received 23 March 2024, revised 30 October 2024
Accepted for publication 5 November 2024
Published 25 November 2024

Abstract

Characterizing materials under shock loading has been of interest in fields such as protective material development, biomechanics to study the injury mechanics and high-speed aerodynamic structures. However, shock loading of material is a very short duration phenomenon and it is extremely challenging to develop sensors for dynamic measurements under such loading conditions. Optical fiber sensors present the possibilities to allow high resolution measurement of displacement in such high strain rate loading conditions. This work studies the possibility of using a fiber-optic loop sensor (FOLS) based on the principle of power losses from the curved section for dynamic measurements under shock loading conditions. The displacement results obtained from the optical sensors are compared with the traditional strain gauge and digital image correlation (DIC) measurements. The result obtained by the FOLS closely matched the sensitivity and precision of the strain gauges and had higher precision than that of DIC.

Keywords: optical fiber, optical sensor, sensor, dynamic measurement, displacement determination

1. Introduction

High *Q*-factor, large dynamic displacement measurement range from micro to millimeter, and long-term stability make fiber-optic sensors (FOS) attractive in force, displacement, vibration and temperature measurements [1–3]. These sensors are relatively immune to electromagnetic interference, which is a major advantage over electrical sensors [4, 5]. The small diameter of optical fibers and flexible nature allows conducting measurements in confined spaces [6] and low cost sensors can be developed for such measurements [7]. Several unique challenges are involved in developing sensors for dynamic measurements. Factors such as fatigue, viscoelasticity, and environmental exposure can lead to a shift in the signal over time. A review of optical sensors available for vibration measurement provides an overview of available sensors, their working principles and application domains [8]. Development of low-cost sensors that can provide dynamic measurements with very short response time remains a challenge, which is addressed in the present work by developing a FOS for displacement determination in shock test experiments.

FOS have been developed based on the principle of optical power loss from a curved section. For example, microbend sensors use a multi-mode optical fiber containing microbends in a localized area to cause power losses. Applied stress or displacement change the bend radius and the resulting power loss, which is calibrated to conduct the measurement. Large size of such sensors remains a challenge in finding their practical applications. Another sensor, a fiber-optic loop sensor (FOLS) was developed using a small circular loop in a single mode optical fiber. This sensor provides the benefit of small size and

* Author to whom any correspondence should be addressed.

high measurement resolution for force and displacement [9–12]. In FOLS, the optical power loss in the transmitted signal depends on the loop radius and also the change in the index of refraction of the fiber material due to the applied stress. The sensor calibration curve shows a general trend of an increase in the optical power loss with decreasing radius of the curved section. However, finer measurements show whispering gallery model resonance peaks resulting in localized high intensity in the transmitted signal at certain loop radii. These peaks appeared by coupling of the modes reflecting back from the cladding-coating interface to the fiber core with the incident modes. This combination of effects was used to develop the sensors to conduct lower resolution measurements in large displacement range and high-resolution measurements in small displacement range. The principle of displacement determination was used to further develop the sensor for vibration measurement [13]. The vibration measurements were conducted in a wide frequency range and the sensor was also validated with measurements of natural frequencies of composite materials.

The theory defining the working principle of FOLS was refined in [14], where flexibility in the fiber was introduced in the equation to improve the predictions of the power loss. FOLS has also been used for temperature measurement [15]. A sensing element design was presented that included a beam of high coefficient of thermal expansion, which caused deformation in the FOLS and allowed calibrating the sensor for temperature measurement with high accuracy.

Development of sensors for fast phenomena such as shock deformation has been a challenge. In the literature, two popular measurement techniques are used for strain measurement in structures loaded by shock waves. The first one is the contact type sensor or strain gauge that provides the displacement determination [16–20]. Strain gauges are bonded to the specimen surfaces for displacement determination with respect to time [21–23]. However, strain gauges require surface preparation and bonding with the substrate using an adhesive, which is not always possible. In addition, it requires the additional calculations and understanding of the structure behavior to determine the displacement result. The bonding area of FOLS is only a point versus a large surface area in the strain gauge. However, one of the major advantages is that FOLS can be attached to measure the displacement on the surface deformed in the range ranging from few microns to several millimeters [9–11], while strain gauge can provide strain measurements on the surface deformed up to hundreds of micrometers [24]. The second option is digital image correlation (DIC), which is a non-contact measurement method [16, 25–28]. DIC is conducted by recording the images of the specimen surface on which a tracking pattern is painted, which leads the advantage in displacement and strain field calculation [29]. However, some disadvantages still exist. Firstly, the object needs to have a line of sight to install a camera, which is not always possible due to the closed end of the shock tube. Secondly, its measurement accuracy depends on the image resolution and data acquisition frequency. These factors may not always be favorable to carry out the high-precision measurement of high-frequency vibrations [30–32].

The aim of this work is to explore the possibility of using FOLS to determine the displacement under shockwave loading conditions, where the equipment requires protection, and have a quick response to capture all ranges of displacements as well. An aerodynamic shock tube is used for the experiments of shock loading of the carbon fiber reinforced polymer (CFRP) composite plate. To find the potential of FOLS, the displacement results obtained by the FOLS were compared with the results of the other contact measurement method, strain gauge, and the contactless method, DIC in the displacement range from micro to millimeter.

2. Experimental design

2.1. FOLS

The operating principal of a FOLS involves measuring optical power losses caused by the deformation of the a loop of smaller than critical radius created in a single mode optical fiber. Under the mechanical deformation, the optical power in the core leaks through the cladding and coasting layers that reduces the transmitted power through FOLS. The loss of power transmission (P^{o}) through an undeformed FOLS defined by the ratio between the output power (P^{o}_{out}) and input power (P_{in}) is a constant. For the deformed FOLS, the power transmission (P) is defined by the ratio between the output power of deformed loop (P_{out}) and input power (P_{in}). Thus, the relative loss of power transmission is given as $P/P^{o} = P_{out}/P^{o}_{out}$, and it is considered as the function of P_{out} with respect to the displacement while P^{o}_{out} is a constant. Nguyen and Gupta [9] provides more detailed explanation of the theory behind FOLS. SME28E optical fiber was curved in a loop of 25 mm radius to construct FOLS. When the optical fiber sensor was fixed, the sensor was calibrated before taking measurements.

Figure 1(a) depicts the calibration setup used to define the relationship between the output optical power P_{out} and compression distance. A Thorlabs DET410 photodetector was used to measure P_{out} in voltage after transmitting through FOLS, which was generated by A Thorlabs S1FC1310 laser source. A data acquisition board (National Instruments DAQ NI USB-6221) connected to a computer acquired the signal from the photodetector using LabView. A stepper motor (Thorlabs MTS25/M) applied displacement at a constant rate of 0.5 mm s^{-1}, which was used to calibrate the FOLS in the existing literature [9, 13–15]. Figure 1(b) shows the output power P_{out} with respect to displacement for the FOLS. The displacement up to 2 mm, as plotted in figure 1(c) inset, was selected for a linear calibration. The CFRP composite back plate later used in the experiments deformed within this range. During the experiment, the relationship P_{out} and displacement was assumed to be linear within 2 mm displacement and was calibrated as

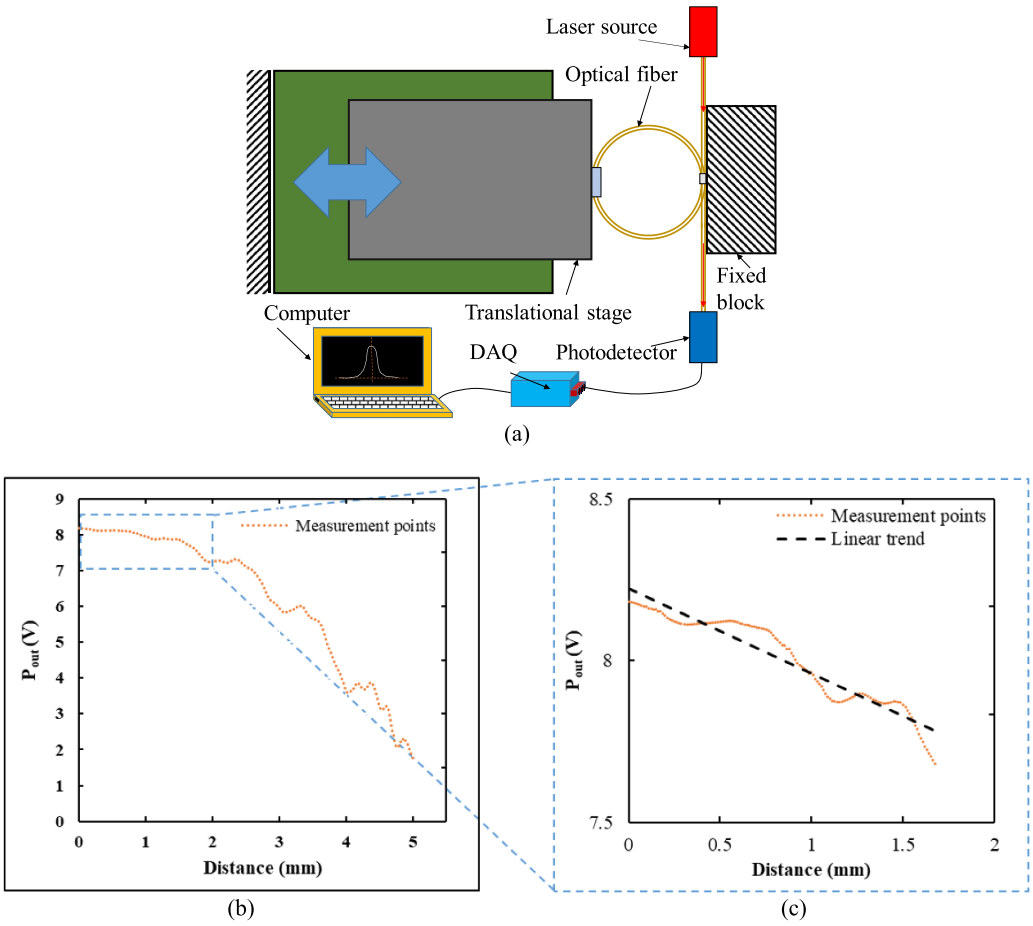

Figure 1. (a) Schematic diagram of calibration experiment for a FOLS. (b) The output optical power $\boldsymbol{P}_{\text{out}}$ with respect to the FOLS displacement at the loading rate of 0.5 mm s^{-1}. (c) The relationship between $\boldsymbol{P}_{\text{out}}$ and distance was assumed to be linear and was calibrated within 2 mm displacement.

$$P_{\text{out}} = a \times \text{displacement} + b \tag{1}$$

where a and b are the two calibration coefficients.

2.2. Experimental platform and test material

The shock tests are conducted using a double-diaphragm pneumatic shock tube (figure 2). The end of the shock tube was covered with a unidirectional CFRP plate procured from Allred and Associates (Elbridge, NY). The length, width, and thickness of the plate are 70, 50 and 1.6 mm respectively. The properties of this CFRP plate are available in the published literature [33]. The shock tube contained two driver and one driven sections that were separated by two scored brass diaphragms designed to rupture in the pressure range of 1.5–7 MPa. There was a tapered section following the second driver chamber to reduce the diameter from that of driver chambers, 50.8 mm, to 25.4 mm for the driven chamber. The shock wave was generated after two diaphragms busted serially due to the pressure difference in two driver chambers. This incident shock wave was accelerated before propagating in the driven chamber. The shock wave pressure was measured by a pressure sensor (PCB Piezotronics 101A06), which was installed on the driven chamber wall and located at 63 mm away from the CFRP specimen. Figure 2(b1) depicts the propagation of the incident shock wave. According to the shock wave theory, the velocity of the incident shock wave is calculated by [34, 35]

$$W_{\text{s}} = M_{\text{s}} c_1 \tag{2}$$

where c_1 is the velocity of sound and M_{s} is the Mach number of the incident shock wave, which can be obtained by

$$\frac{p_2}{p_1} = \frac{2\mu M_{\text{s}}^2 - (\mu - 1)}{\mu + 1} \tag{3}$$

where p_1 and p_2 are the absolute pressure at room temperature and the absolute pressure behind the incident shock front, respectively. μ is the specific heat coefficient, taken as 1.4 in the experiment [34]. The shock wave component reflected with the reflected velocity W_{r} from the CFRP specimen installed at the end of the driven chamber led to a pressure p_5, as shown in figure 2(b2). Figure 2(c) shows the acquired pressure applied to the plate over time, where it is observed that p_5 is significantly higher than p_2. The vibration of the CFRP specimen due to its interaction with the shock wave was simultaneously

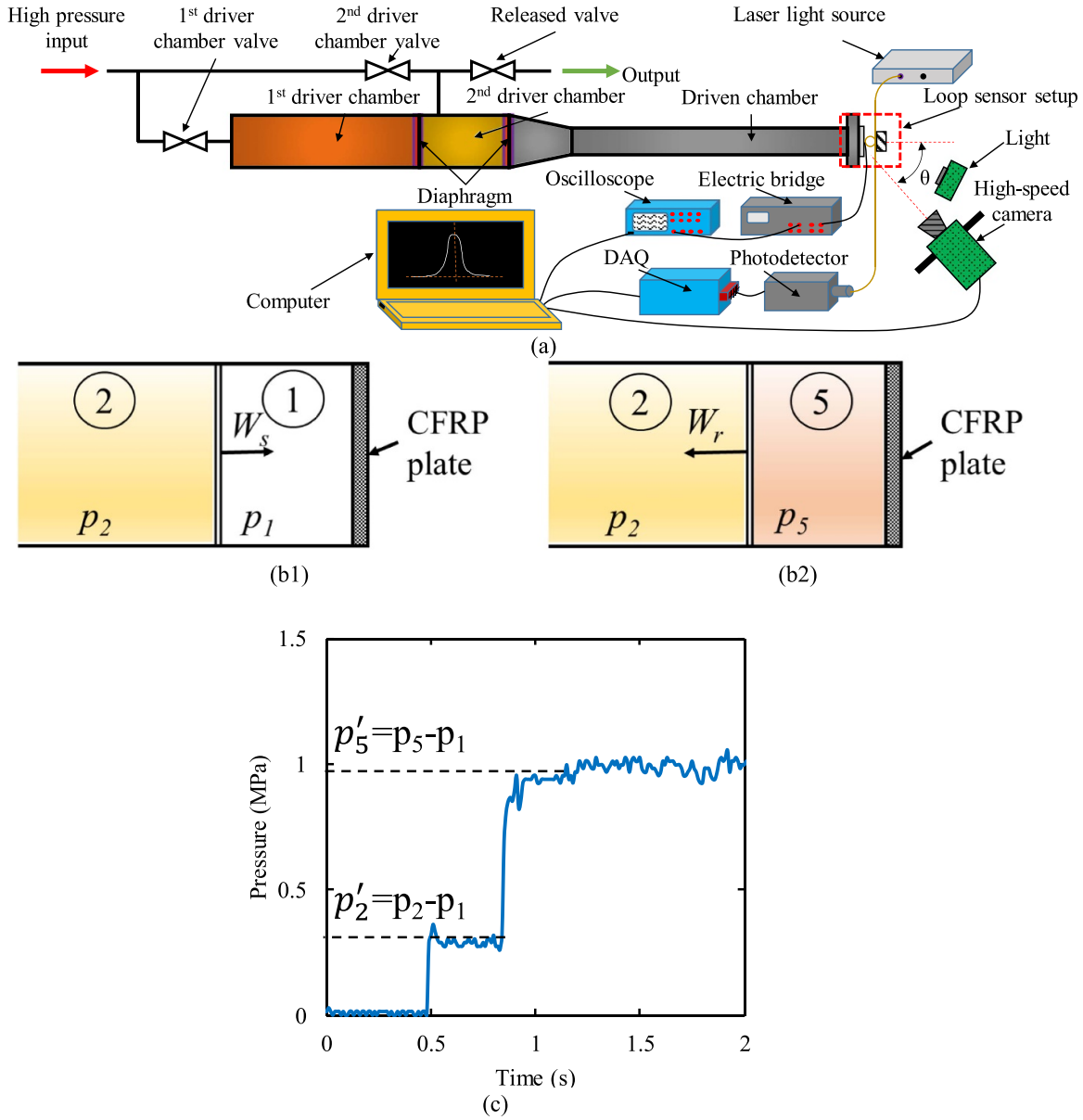

Figure 2. (a) Schematic diagram of the shock tube experimental setup. The propagation of (b1) the incident shock wave and (b2) the reflected shock wave after impacting the CFRP. (c) The pressure signal before and after the shock wave impacted the CFRP plate.

captured by three measurement methods: FOLS, strain gauge, and DIC.

The placement of strain gauge and FOLS in the experimental system is shown in figure 3. The strain gauge was mounted on the CFRP surface and a speckle pattern for DIC was painted as well. The detailed process steps of strain gauge and DIC measurements are presented in the following sections. Finally, the FOLS was mounted as illustrated in figure 3(b) and glued on top of the strain gauge. The hollow tube was used tightly secured to the optical fiber to keep the sensor from changing the circumference of the measurement portion of the optical fiber during measurement. The contact region between the FOLS, strain gauge and CFRP specimen was glued firmly in order to maintain their contact when the plate oscillated. In this work, the parameters of shock wave and FOLS's calibration coefficients of all case studies are listed in table 1.

2.3. Processing of strain gauge data

Figure 4 shows the installation diagram to determine the maximum deflection of CFRP plate using the strain gauge. The 11.1 × 3.81 mm strain gauge (Micro-Measurements MMF335442) was glued firmly at the center of the CFRP plate. The voltage signal of the strain gauge was amplified by the strain gauge conditioner before being recorded by the oscilloscope (Tektronix TDS 2014B). In order to calculate the deflection at the central point of plate, the model of the beam fixed at both ends was developed as illustrated in figure 4.

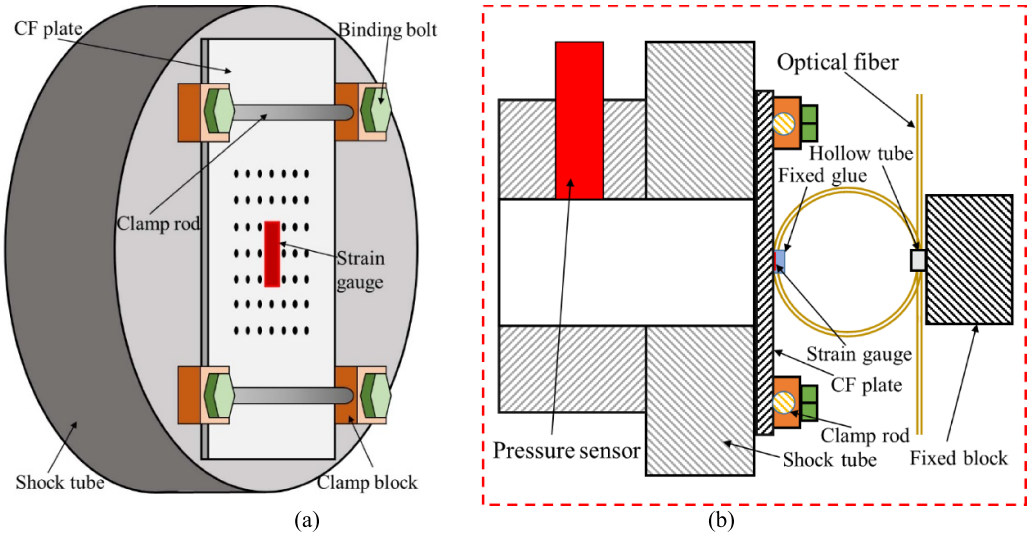

Figure 3. (a) CFRP plate installed at the end of the shock tube containing speckle pattern and strain gauge and (b) the FOLS on the side view. The figure is not drawn to scale.

Table 1. Study to calibrate the coefficients of FOLS.

Case	Incident shock wave velocity (m s^{-1})	Reflected shock wave pressure (Pa)	Calibration coefficients of FOLS	
			a	b
1	626	9.25×10^5	0.2635	8.2244
2	637	9.54×10^5	0.2648	8.2238
3	640	9.39×10^5	0.2603	8.2221

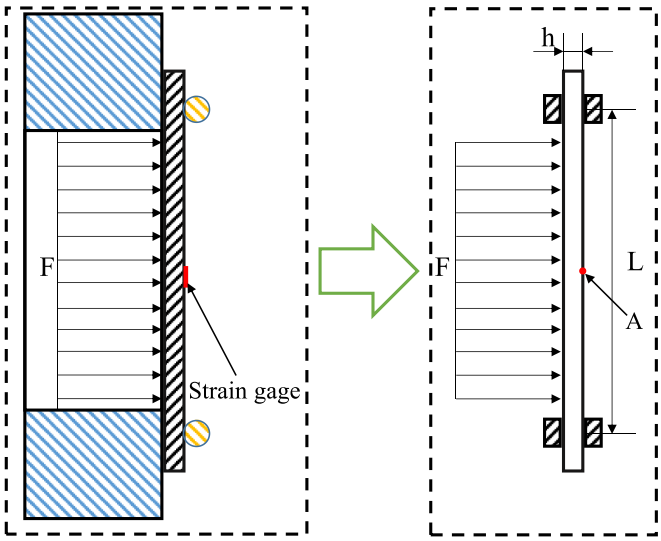

Figure 4. The model of load applied to the CFRP plate.

The pressure p of the reflected shock wave was assumed as a uniformly distributed load on the beam. For elastic deformation, the deflection d, stress σ, and the moment M at the central point are obtained by [36]

$$d = \frac{pL^4}{384EI_z} \tag{4}$$

$$\sigma = \frac{Mh}{2I_z} = E\varepsilon \tag{5}$$

$$M = \frac{pL^2}{24} \tag{6}$$

where h and I_z are the thickness and the second moment of area of the beam, respectively. E is the elastic modulus of the beam, and ε is the strain data measured at the central point. Finally, the relationship between ε and the deflection d are given by inserting equations (4) and (5) into equation (6) as

$$d = \frac{L^2}{8h}\varepsilon. \tag{7}$$

In equation (7), the thickness h is also the thickness of the CFRP plate (1.6 mm) and the effective span length L is 53 mm.

2.4. Processing of high-speed camera image

Figure 5(a) shows the 2D speckle pattern grid marked to trace the deformation of the CFRP plate. It is a symmetric speckle pattern. The movement of these speckle points was recorded by the high-speed camera (NAC MEMRECAM HX-5) that was set up as shown in figure 5(b). The high speed camera is installed at the same height as the center of the CFRP plate.

The frame rate of the high-speed camera was set to 7000 Hz for all test cases. Since the high-speed camera was installed at the angle θ, the horizontal distance h_s between two points was

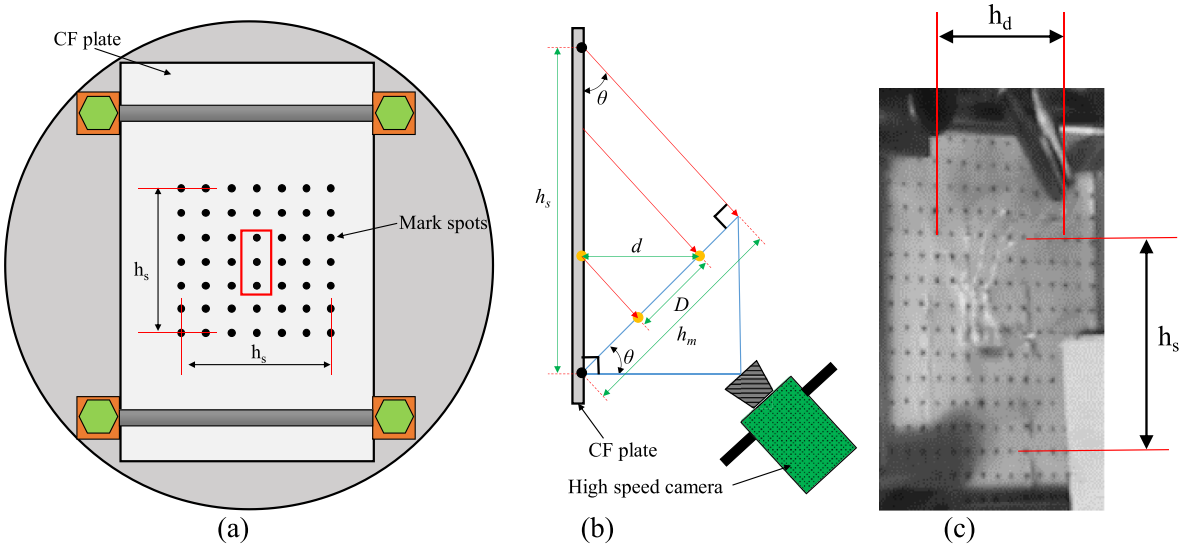

Figure 5. (a) The DIC tracking point pattern was painted on the CFPR plate. (b) Schematic diagram of the DIC experimental setup. (c) The high speed camera image of the CFRP plate.

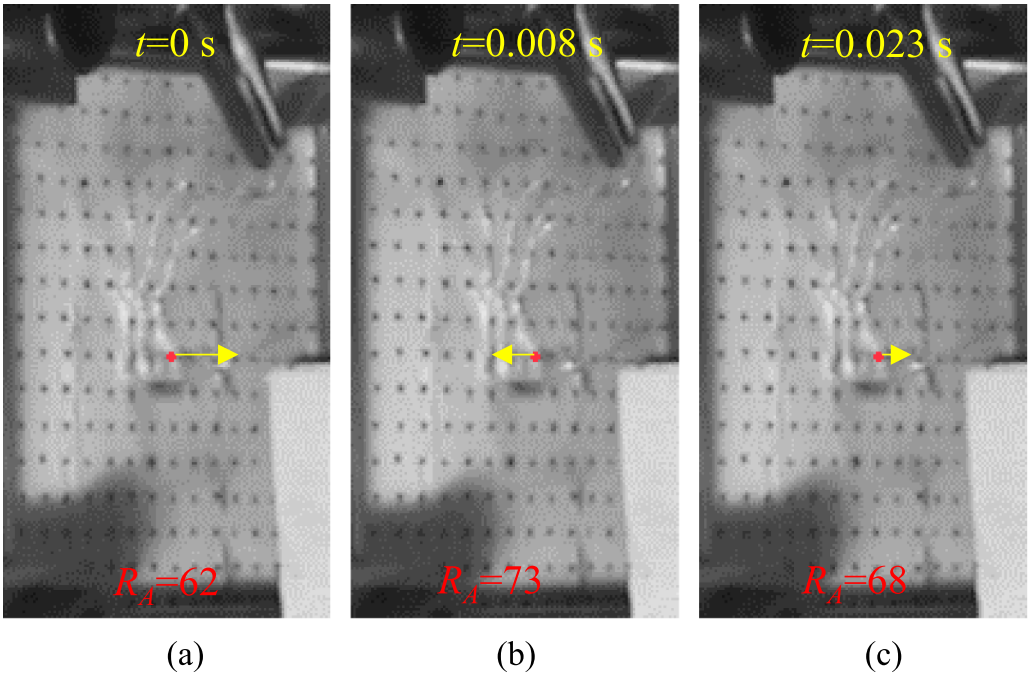

Figure 6. The high speed camera images capturing the CFRP plate's deflection under the impact of the 637 m s^{-1} incident shock wave at t = (a) 0, (b) 0.008 s and (c) 0.023 s. The respective R_A values at these time instances are measured as 62, 73 and 68, respectively.

captured as h_d as shown in figure 5(c). The camera angle θ was used in the following equation:

$$\sin\theta = \frac{h_d}{h_s}. \tag{8}$$

In this work, the camera angle θ was calculated as 38.1°. Suppose that the distance that the tracking points moved after the impact of the shock wave was measured in the image is D, the deflection d of the CFRP plate was defined by

$$d = D/\cos\theta. \tag{9}$$

Figure 6 showed a results of high-speed camera images capturing the CFRP plate's deflection under the impact with frame rate of 7000 Hz or 1.43 × 10^{-3} s. The position of the central point A was tracked at different times and its horizontal pixel value (R_A) of point A was extracted from the images to convert to the distance D. In these images, one horizontal pixel was correlatedly converted to 0.145 mm. The CFRP plate central point reached the first peak (maximum deflection) and the second one at 0.008 s and (c) 0.023 s, respectively.

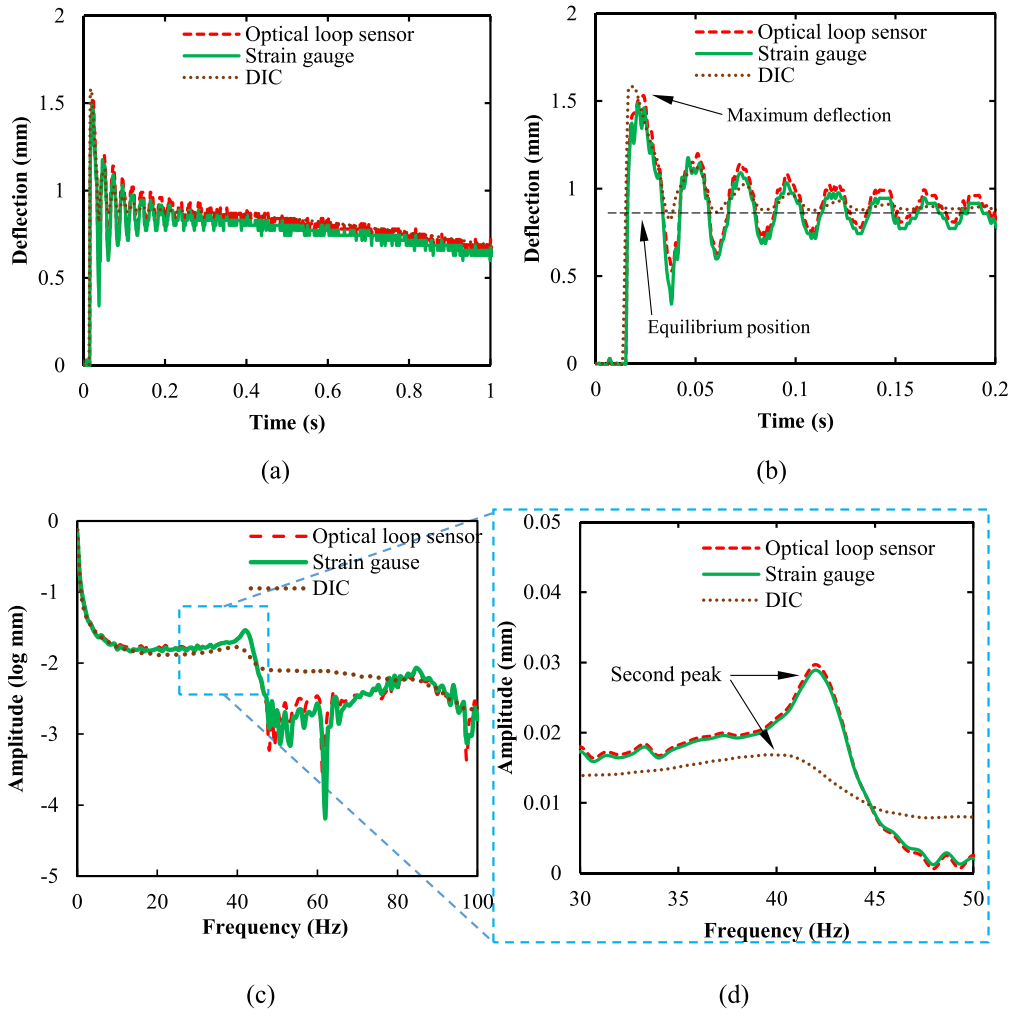

Figure 7. (a) Deflection at the central point of the CFRP plate under the impact of the 637 m s^{-1} incident shock wave. (b) The oscillation at the central point and (c) its frequency on the logarithm scale, (d) closer view of frequency.

3. Results and discussions

After converting the measurement data to deflection, the experimental results on displacement, measured by three different methods including the FOLS, strain gauge, and DIC, are shown in figure 7. In figure 7(a), all three methods successfully captured the deflection at the central point of the CFRP plate that deformed under the impact of the 637 m s^{-1} incident shock wave. The movement of the central point of the CFRP plate can be observed into three separate steps. In the first step, the CFRP plate rapidly deformed under increasing pressure on its surface when the reflected shock wave was generated, and its central point reached the maximum deflection. In the next one, the central point decadently oscillated around the equilibrium deflected position before steadily returned to the equilibrium position in the last step. Figure 7(b) provides a detailed view of the oscillation and its dissipation in the first and second steps. The similar oscillation pattern was found in the separated study of composite plates [16, 28].

In the second step, all three methods captured the decadent oscillations at the central point but there was a difference in the time to reach the equilibrium position. In comparison, the results of decay rate and oscillation magnitudes were similar with the FOLS and strain gauge, but the decay rate was found higher with DIC. This difference can be explained by the limitation of image resolution that is reduced to increase the frame rate. In figure 7(b), the oscillation magnitudes obtained by FOLS and strain gauge decreased below 0.2 mm after six cycles. It led difficulty in recognizing the oscillation at the central point by DIC because 1 pixel corresponded to 0.145 mm in the high speed camera images. In addition, the error in measuring the oscillation magnitude by DIC existed in the range of the pixel-length conversion. However, the frequency of the oscillation at the central point was defined consistently by all three methods, as shown in figure 7(c) where its magnitude was plotted on the logarithm scale. The fast Fourier transform was used to convert the time domain data in figure 7(b) to the frequency domain in figure 7(c). Two peaks were seen from the curve of

Table 2. Experimental results measured at the central point of the CFRP plate by three methods.

Measurement quantity	Case	Strain gauge	FOLS	DIC	Error of FOLS (%)	Error of DIC (%)
Maximum deflection (mm)	1	1.42	1.45	1.6	2.1%	12.7%
	2	1.49	1.56	1.57	4.7%	5.4%
	3	1.48	1.53	1.52	3.4%	2.7%
Equilibrium position (mm)	1	0.79	0.89	0.87	12.7%	10.1%
	2	0.86	0.88	0.94	2.3%	9.3%
	3	0.83	0.84	0.79	1.2%	−4.8%
Frequency (Hz)	1	41.5	41.5	41.2	0.0%	−0.7%
	2	41.6	41.7	40.9	0.2%	−1.7%
	3	41.1	41.2	40.8	0.2%	−0.7%

the FOLS. Figure 7(d) provided the closer view of the second peak. The first peak frequency of 0 Hz corresponded to the equilibrium deflected position, and the second one was for the decadent oscillation around the equilibrium position. The similarity was found in the strain gauge and DIC results.

The results of maximum deflection, equilibrium position and second peak frequency measured at the central point of the CFRP plate by three methods are listed in table 2. The equilibrium position was calculated by the average value of the maximum and minimum of the sixth periods. The results from the strain gauge were used as the baseline to calculate the error for the FOLS and DIC results. In general, the FOLS provided more consistent results with the strain gauge than the DIC. Especially, the agreement in the frequency of the decadent oscillation in the second step seems good with the error less than 0.2%. This consistent result shows that the FOLS signal was not affected by the self-vibration of loop-shape during the deformation. From the above comparison, it can be seen that the FOLS can carry out the high-precision measurement for objects deformed under the dynamic load.

4. Conclusions

In this work, the FOLS successfully measured the CFRP plate's behavior under shock loading. Other two measurement methodologies including the strain gauge and DIC were conducted to compare the displacement results with the ones of FOLS. The FOLS successfully captured three deflection steps of the central point of the CFRP plate under shock loading. The consistent results were also found with the strain gauge and DIC methods. The decadent oscillation at the central point of CFRP plate was reliably measured by the FOLS. In the comparison, the result obtained by the FOLS was as similar as the one of the strain gauges in capturing all vibrations up to 100 Hz, especially, the second peak frequency error is less than 0.2%. The FOLS provided more precise results than the DIC. Notably, the frequency measurements obtained by the FOLS were unaffected by the self-vibration of the loop shape during deformation. Based on the successful performance of FOLS in this work, it is recommended as an alternative for applications that require displacement determination under dynamic loadings. Due to capability of high sensitivity and precision measurement, FOLS seems to be a promising technology for applications requiring high-strain rate and short duration phenomena.

Data availability statement

All data that support the findings of this study are included within the article.

Acknowledgment

The support by the Mechanical and Aerospace Engineering Department at NYU Tandon School of Engineering is gratefully acknowledged.

The author Nikhil Gupta acknowledges National Science Foundation Grant OISE-1952479 for partially supporting him to contribute to this work.

Ethical statement

No conflict of interest is declared by the authors. All authors have contributed significantly to the work and have read and approved the final manuscript. Any errors or omissions are the responsibility of the authors. The authors certify that they have no affiliations with or involvement in any organization or entity with any financial interest or non-financial interest in the subject matter or materials discussed in this manuscript.

ORCID iD

Dung Dinh Luong https://orcid.org/0000-0002-8624-8845

References

[1] Fu D Y, Liu X, Shang J, Sun W and Liu Y 2020 A simple, highly sensitive fiber sensor for simultaneous measurement of pressure and temperature *IEEE Photonics Technol. Lett.* **32** 747–50

[2] Mao Y, Ashry I, Hveding F, Bukhamsin A Y, Hong Y, Ng T K and Ooi B S 2020 Simultaneous distributed acoustic and temperature sensing using a multimode fiber *IEEE J. Sel. Top. Quantum Electron.* **26** 7

[3] Dedyulin S, Todd A, Janz S, Xu D-X, Wang S, Vachon M and Weber J 2020 Packaging and precision testing of fiber-Bragg-grating and silicon ring-resonator thermometers: current status and challenges *Meas. Sci. Technol.* **31** 7
[4] Milne D, Masoudi A, Ferro E, Watson G and Le Pen L 2020 An analysis of railway track behaviour based on distributed optical fibre acoustic sensing *Mech. Syst. Signal Process.* **142** 15
[5] Li X F, Zhang H, Qian C, Ou Y, Shen R and Xiao H 2020 A new type of structure of optical fiber pressure sensor based on polarization modulation *Opt. Lasers Eng.* **130** 6
[6] Acker C D, Yan P and Loew L M 2020 Recent progress in optical voltage-sensor technology and applications to cardiac research: from single cells to whole hearts *Prog. Biophys. Mol. Biol.* **154** 3–10
[7] Leal A *et al* 2020 Low-cost and high-resolution pressure sensors using highly stretchable polymer optical fibers *Mater. Lett.* **271** 127810
[8] Shao L, Liu S, Bandyopadhyay S, Yu F, Xu W, Wang C, Li H, Vai M I, Du L and Zhang J 2020 Data-driven distributed optical vibration sensors: a review *IEEE Sens. J.* **20** 6224–39
[9] Nguyen N Q and Gupta N 2009 Power modulation based fiber-optic loop-sensor having a dual measurement range *J. Appl. Phys.* **106** 033502.1–033502.5
[10] Gupta N and Nguyen N Q 2013 *Fiber-optic Extensometer* (Polytechnic Institute of New York University)
[11] Gupta N and Nguyen N Q 2014 *Method for Measuring the Deformation of a Specimen Using a Fiber Optic Extensometer* (Polytechnic Institute of New York University)
[12] Yang Y, Chen K and Gupta N 2018 Fiber-optic sensors *Material-Integrated Intelligent Systems - Technology and Applications* (Wiley) pp 107–36
[13] Nishino Z T, Chen K and Gupta N 2014 Power modulation-based optical sensor for high-sensitivity vibration measurements *IEEE Sens. J.* **14** 2153–8
[14] Yang Y, Averardi A and Gupta N 2019 Power modulated fiber-optic loop sensor: theoretical and experimental investigation *IEEE Sens. J.* **19** 1813–9
[15] Yang Y, Averardi A and Gupta N 2019 An intensity modulation based fiber-optic loop sensor for high sensitivity temperature measurement *Sens. Actuators* A **297** 8
[16] Jahnke D, Yildiz S and Andreopoulos Y 2018 Embedding sensors in composite plates for characterization under impacting shock wave loading *J. Compos. Mater.* **52** 3831–50
[17] Gong M and Andreopoulos Y 2008 Shock wave impact on monolithic and composite material plates: the preferential aeroelastic response *J. Sound Vib.* **313** 171–94
[18] Yildiz S, Andreopoulos Y, Delale F and Smail A 2020 Adhesively bonded joints under quasi-static and shock-wave loadings *Int. J. Impact Eng.* **143** 103613
[19] Stoffel M, Schmidt R and Weichert D 2001 Shock wave-loaded plates *Int. J. Solids Struct.* **38** 7659–80
[20] Stoffel M 2006 A measurement technique for shock wave-loaded structures and its applications *Exp. Mech.* **46** 47–55
[21] Gorbushin A R and Bolshakova A A 2020 *Unsteady Axial Force Measurement by the Strain Gauge Balance* vol 152 (Measurement) p 8
[22] Weiland J, Sadeghi M Z, Thomalla J V, Schiebahn A, Schroeder K U and Reisgen U 2020 Analysis of back-face strain measurement for adhesively bonded single lap joints using strain gauge, Digital Image Correlation and finite element method *Int. J. Adhes. Adhes.* **97** 8
[23] Dai X J, Ye H, Yuan T, Shao X, Zu Z, Cheng X, Yun H, Wang Y, Yang F and He X 2020 Strain determination based on strain gauge-guided radial basis function and digital image correlation *Opt. Lasers Eng.* **126** 11
[24] Micro-Measurements 2015 *Precision Strain Gages and Sensors* (available at: https://vishay-straingauge.com/pdf/strain/precision-strain-gages-sensors-1.pdf)
[25] LeBlanc J and Shukla A 2011 Dynamic response of curved composite panels to underwater explosive loading: experimental and computational comparisons *Compos. Struct.* **93** 3072–81
[26] Kumar P, Stargel D S and Shukla A 2013 Effect of plate curvature on blast response of carbon composite panels *Compos. Struct.* **99** 19–30
[27] Tekalur S A, Shukla A and Shivakumar K 2008 Blast resistance of polyurea based layered composite materials *Compos. Struct.* **84** 271–81
[28] Pankow M, Justusson B, Salvi A, Waas A M, Yen C-F and Ghiorse S 2011 Shock response of 3D woven composites: an experimental investigation *Compos. Struct.* **93** 1337–46
[29] Pan B 2018 Digital image correlation for surface deformation measurement: historical developments, recent advances and future goals *Meas. Sci. Technol.* **29** 082001
[30] Liu B, Yang J and Gang T 2020 Analysis of sound and vibration interaction on a crack and its use in high-frequency parameter selection for vibro-acoustic modulation testing *Mech. Syst. Signal Process.* **143** 11
[31] Li Y W *et al* 2020 A novel high-frequency vibration error estimation and compensation algorithm for THz-SAR imaging based on local FrFT *Sensors* **20** 13
[32] Sun Z S, Liu K, Jiang J, Ma P, Wang S, Xu Z, Guo H, Zhou Z, Xu T and Liu T 2020 Distributed vibration sensing with high frequency response by using WDM based integrated scheme *J. Phys. D: Appl. Phys.* **53** 7
[33] Xu X and Gupta N 2019 Artificial neural network approach to determine elastic modulus of carbon fiber-reinforced laminates *JOM* **71** 4015–23
[34] Henshall B D 1955 *The Use of Multiple Diaphragms in Shock Tubes* (Aeronautical Research Council Current Papers)
[35] Alpher R A and White D R 1958 Flow in shock tubes with area change at the diaphragm section *J. Fluid Mech.* **3** 457–70
[36] Meriam J 2019 *Engineering Mechanics: Statics* vol 1 (Wiley)